

ADVANCING GEOMETRIC CONJUNCTION FILTERS TO HANDLE SATELLITE MANOEUVRES

Ana S. Rivero⁽¹⁾, Rafael Vazquez⁽¹⁾, Klaus Merz⁽²⁾

⁽¹⁾ *Universidad de Sevilla, Escuela Técnica Superior de Ingeniería, Camino de los Descubrimientos s.n. 41092 Sevilla (Spain), Email: {asanchez8, rvazquez1}@us.es*

⁽²⁾ *Space Debris Office, ESA/ESOC, Robert-Bosch-Str. 5, 64293 Darmstadt, Germany, Email: Klaus.Merz@esa.int*

ABSTRACT

The exponential growth of Resident Space Objects (RSOs) has significantly increased the computational demands of conjunction analysis, essential for space traffic management. Conjunction filtering processes, which eliminate RSO pairs unlikely to collide, are widely used to reduce this complexity. However, existing geometric filters suffer from two key limitations: they often neglect some perturbative effects on orbital elements and fail to account for satellite manoeuvres.

This study enhances the Space Occupancy (SO) and Space Occupancy Path (SOP) filters by integrating satellite manoeuvres and atmospheric drag effects. Atmospheric drag is modelled using King-Hele's theory to estimate orbital decay, while manoeuvres are addressed through ephemeris-based real-time position updates.

The proposed filters improve the fidelity of conjunction analysis while preserving computational efficiency, addressing critical challenges posed by the escalating satellite population and advancing sustainable practices for orbital safety.

1 INTRODUCTION

The increasing congestion in the near-Earth space environment presents unprecedented challenges for sustainable space traffic management and orbital safety. The “new space era” is characterized by exponential growth in Resident Space Objects (RSOs), driven by both the deployment of extensive satellite constellations and the proliferation of space debris [16]. This situation has transformed Conjunction Analysis (CA) from a specialized concern into a critical necessity for ensuring the long-term sustainability of space activities.

CA serves as an essential tool in space traffic management, encompassing methodologies and processes designed to evaluate and mitigate collision risks in orbit. While current operational practices primarily focus on the *one-vs-all* conjunction screening problem [11], this approach addresses only a fraction of the collision risk landscape. The more comprehensive *all-vs-all* conjunction screening problem, which

examines potential collisions among all catalogued Resident Space Objects (RSOs), remains a significant challenge [20].

The computational complexity of the *all-vs-all* problem is staggering and is expected to intensify even more with the increasing number of catalogued objects being tracked. Nonetheless, prior research has explored various strategies to address these computational challenges, with conjunction filter processes being among the most widely used acceleration techniques. These filters efficiently eliminate pairs of RSO with negligible collision risk, significantly reducing the computational load of detailed CA.

These processes typically involve a series of successive filters. The classical method proposed by Hoots [10] starts with the apogee-perigee filter, followed by the orbit path filter, which are based on the geometry of the orbit and the geometry of the pair, respectively. These filters are referred to as geometric filters for this reason, as they do not consider the position of the satellite in orbit. This aspect is considered by the third and final filter of the process, the time filter.

Geometric filters have classically had two main limitations. The first is their reliance on a Keplerian framework; perturbations lead to variations in orbital elements, which in turn cause alterations in the geometry of the orbits. The second significant issue is their failure to account for the possibility of executing manoeuvres, which is crucial when at least one of the objects is an active satellite. The latter is becoming increasingly relevant due to the growing population of active satellites.

Previous studies have sought to address these challenges by investigating diverse filtering processes [22, 4, 7]. For instance, Casanova et al. in [4] utilize ephemeris tables to obtain equinoctial orbital elements, which are then linearly interpolated to estimate these elements at a given time. Alfano, in his work [1], introduces a geometric approach, offering versatility by enabling users to specify different in-plane and out-of-plane bounds for the path filter. Additionally, buffer distances are often incorporated into conjunction filters to reduce false positives, though they must be carefully calibrated to balance accuracy and efficiency [2].

The authors previously developed two novel filters in their earlier works [18] and [17]: the Space Occupancy filter (SO-filter), which serves as an alternative to the classical apogee-perigee filter, and the Space Occupancy Path filter (SOP-filter), which offers a distinct approach compared to the classical orbit path filter. The key advantage of these filters lies their foundation on a zonal-perturbed two-body problem model.

The purpose of the present work is to adapt these filters, which already account for zonal harmonics perturbations to be further tuned as objects manoeuvre during the prediction time span. Additionally, this work incorporates the atmospheric drag effect, since it is one of the most relevant perturbations, along with zonal harmonics—in Low Earth Orbit (LEO). The manoeuvre issue is addressed by using ephemeris files, which allow for the updating of real satellite data to handle manoeuvres that change the altitude of the orbit. Regarding atmospheric drag, the orbital model for a spherically symmetrical, exponential atmosphere of King-Hele is used [12] to analytically model the reduction in altitude experienced by low-eccentricity orbits due to this perturbation. This enables the analytical estimation of the reduction in the semimajor axis and consequently, the decrease in the minimum radius.

These improvements have been numerically validated using Starlink constellation. The filter process has been applied by confronting the satellites of the constellation in an *all-vs-all* approach.

The structure of this paper is as follows: After this introduction, a brief explanation of the Space Occupancy filter process is performed in Section 2. The implementations developed in this work are presented in Section 3, detailing how the filters have been tuned to account for satellite manoeuvres, and Section 4 covers the implementation of the atmospheric drag. Section 5 presents the implementation of the improved filters, and the five different configurations used to validate the new methods. Finally, Section 6 presents validation tests on the Starlink constellation. The paper concludes in Section 7 with some final remarks and suggestions for future work.

2 SPACE OCCUPANCY FILTER PROCESS

The Space Occupancy filter process consists of two geometric filters, the SO-filter and the SOP-filter, which are based on the principles of the apogee-perigee filter and the path filter, respectively. The key aspect of these filters is that they are able to account for the effect of zonal harmonics. To achieve this, Space Occupancy (SO) concept [3] and Cook's theory are employed [5, 6].

The Space Occupancy (SO) concept is described as the domain occupied by an individual satellite as it moves

along its nominal orbit under the effects of environmental perturbations during a given interval of time [3]. This concept was initially defined for a long-time scale, on the order of the period of the line of apsides. However, time horizons in conjunction analysis are significantly shorter, usually ranging from 5 to 7 days. To address this time discrepancy, a “short-term SO” theory was developed in [18]. It estimates the satellite's altitude range by employing the approximate evolution of the radius for a non-frozen orbit with small eccentricity, using a first-order eccentricity expansion:

$$r \approx \hat{a}(1 - \hat{e} \cos(\hat{\theta} - \hat{\omega})) + \frac{J_2}{4\hat{a}}[(9 + \cos 2\hat{\theta}) \sin^2 \hat{i} - 6] \quad (1)$$

where \hat{a} , \hat{i} , $\hat{\theta}$ and $\hat{\omega}$ represent the mean values, averaged over the mean anomaly, of the semimajor axis, inclination, argument of latitude and argument of periapsis, respectively.

Equation (1) can be reformulated using Cook's theory, which describes the behaviour of the mean eccentricity vector, (ξ, η) , of an orbit influenced by J_2 and an arbitrary sequence of odd zonal harmonics [5], to obtain an expression for the radius as an explicit function of the argument of latitude, $\hat{\theta}$, and time, β ,

$$r(\hat{\theta}, \beta) \approx \hat{a}(1 - e_p \cos(\hat{\theta} - \beta) - e_f \sin \hat{\theta}) + \frac{J_2}{4\hat{a}}[(9 + \cos 2\hat{\theta}) \sin^2 \hat{i} - 6] \quad (2)$$

where e_p , e_f , and β represent the frozen eccentricity, proper eccentricity, and rotation angle respectively. Cook's theory provides the analytical expressions for these parameters, which are written here for the reader's convenience:

$$e_f = k^{-1} a^{-\frac{3}{2}} \quad (3)$$

$$\sum_{n=1}^N \frac{J_{2n+1}}{a^{2n+1}} \frac{n}{(2n+1)(n+1)} P_{2n+1}^1(0) P_{2n+1}^1(\cos \hat{i}),$$

$$e_p = \sqrt{(\hat{e}_0 \sin \hat{\omega}_0 - e_f)^2 + \hat{e}_0^2 \cos^2 \hat{\omega}_0}, \quad (4)$$

$$\sin \alpha = \frac{\hat{e}_0 \sin \hat{\omega}_0 - e_f}{e_p}, \quad (5)$$

$$\cos \alpha = \frac{\hat{e}_0 \cos \hat{\omega}_0}{e_p}, \quad (6)$$

$$\beta(\tau) = \alpha + \kappa \tau, \quad (7)$$

$$\kappa = \frac{3J_2}{\hat{a}^2} \left(1 - \frac{5}{4} \sin^2 \hat{i}\right). \quad (8)$$

P_n^1 denotes the associated Legendre function of the first order and degree n , J_{2n+1} are the odd zonal harmonic coefficients, and τ denotes the dimensionless time considering the Earth's radius as the reference length

unit and $1/n_{\oplus}$ as the reference time, with n_{\oplus} the mean motion of a circular orbit of radius R_{\oplus} . The initial conditions \hat{e}_0 and $\hat{\omega}_0$ represent the mean eccentricity and argument of periapsis at $\tau = 0$.

An accurate and efficient method to compute the maximum and minimum value of Eq. (2) within a specific timeframe is provided by [18]. It involves solving a quartic equation, leveraging the short-term SO model as a computationally efficient tool to accurately compute radial bounds. Figure 1 illustrates the schema of the SO and the radial bounds with the required buffer. These boundaries, R_{max} and R_{min} in Figure 1, are used by the SO-filter to efficiently remove pairs of objects with non-overlapping ranges of radii.

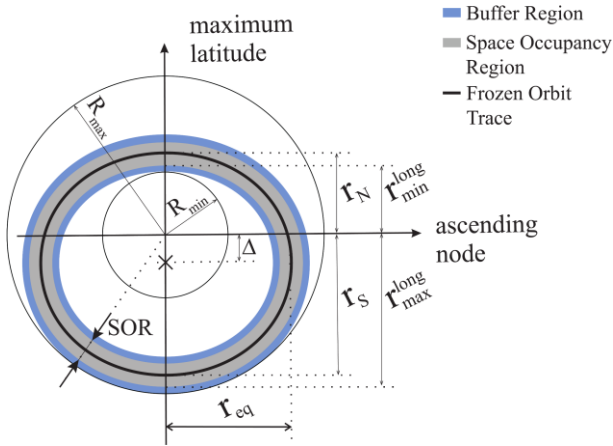


Figure 1. Space Occupancy Geometry [18].

This procedure is also extended to the path filter resulting in the newly introduced SOP-filter. The classical orbit path filter focuses on the concept of minimum orbit intersection distance (MOID), which has been thoroughly investigated in the literature [8, 9]. When the orbits are far from being coplanar, the MOID occurs at the relative nodes [8]. Then, the proposed procedure of the SOP-filter estimates the maximum and minimum value of the orbital radius in a specific timeframe when the object is located at the mutual nodes [17]. These bounds are used by the SOP-filter to efficiently remove pairs of objects with non-overlapping ranges of radii at either of the nodes.

Considering the influence of zonal harmonics, the temporal shift of relative nodes transitions them from discrete points to measurable intervals. The calculation incorporates the influence of the first three zonal harmonics (J_2, J_3, J_4) using the expression for the secular effect of $\hat{\Omega}$, as developed by Kozai in [13].

This second filter employs an approximation of the orbit radius considering up to the third order in eccentricity. Moreover, it uses a more comprehensive theory to describe the behaviour of the mean eccentricity vector, developed in [6], which expands upon this result by

including the impact of the remaining even harmonic. The theory is also modified in [17] to include a correction to account for the effect of the order $J_2 \hat{e}^2$. The radius expression employed by this filter is

$$r(\hat{\theta}, \beta) \approx \hat{a} \left(1 - e_p \cos \hat{\theta} \cos \beta - \sqrt{\frac{\kappa_\eta}{\kappa_\xi}} e_p \sin \hat{\theta} \sin \beta - e_f \sin \hat{\theta} \right) \cdot \left[1 - \left(e_p \sin \hat{\theta} \cos \beta - \sqrt{\frac{\kappa_\eta}{\kappa_\xi}} e_p \cos \hat{\theta} \sin \beta - e_f \cos \hat{\theta} \right)^2 \right] + \frac{J_2}{4\hat{a}} [(9 + \cos 2\hat{\theta}) \sin^2 \hat{\theta} - 6], \quad (9)$$

where some parameters are reformulated as follows

$$C = \sum_{n=1}^N \frac{\hat{n} J_{2n+1}}{a^{2n+1}} \frac{n}{(2n+1)(n+1)} P_{2n+1}^1(0) P_{2n+1}^1(\cos \hat{i}), \quad (10)$$

$$e_f = \frac{C}{\kappa_\xi}, \quad (11)$$

$$e_p = \sqrt{\frac{\kappa_\xi}{\kappa_\eta} (\hat{e}_0 \sin \hat{\omega}_0 - e_f)^2 + \hat{e}_0^2 \cos^2 \hat{\omega}_0} \quad (12)$$

$$\sin \alpha = \frac{\sqrt{\frac{\kappa_\xi}{\kappa_\eta} \hat{e}_0 \sin \hat{\omega}_0 - e_f}}{e_p}, \quad (13)$$

$$\beta(\tau) = \alpha + \kappa_\xi \sqrt{\frac{\kappa_\eta}{\kappa_\xi}} \tau, \quad (14)$$

$$\begin{aligned} \kappa_\xi &= - \sum_{n=1}^N \frac{\hat{n} J_{2n}}{a^{2n}} \left(\frac{2n(2n+1)}{2} P_{2n}(\cos \hat{i}) P_{2n}(0) \right. \\ &\quad \left. + \frac{(2n-1)(2n-2)(2n-2)!}{2(2n+2)!} P_{2n}^2(\cos \hat{i}) P_{2n}^2(0) \right. \\ &\quad \left. - P'_{2n}(\cos \hat{i}) P_{2n}(0) \cot \hat{i} \right), \end{aligned} \quad (15)$$

$$\begin{aligned} \kappa_\eta &= - \sum_{n=1}^N \frac{\hat{n} J_{2n}}{a^{2n}} \left(- \frac{2n(2n+1)}{2} P_{2n}(\cos \hat{i}) P_{2n}(0) \right. \\ &\quad \left. + \frac{(2n-1)(2n-2)(2n-2)!}{2(2n+2)!} P_{2n}^2(\cos \hat{i}) P_{2n}^2(0) \right. \\ &\quad \left. + P'_{2n}(\cos \hat{i}) P_{2n}(0) \cot \hat{i} \right) \end{aligned} \quad (16)$$

As with the SO-filter, this conjunction filter is developed as an optimization problem: determining the maximum and minimum values of the radius function, but with boundaries in both variable—temporal (β) and

argument of latitude ($\hat{\theta}$)—the latter being defined by the relative nodes. Here, the quartic equation of the first filter is replaced by a sixth-degree polynomial equation. Additionally, the constraint of the argument of latitude interval introduces a second polynomial, resulting in a total of two sixth-degree polynomials.

3 INTEGRATION OF MANOEUVRES IN THE FILTERING PROCESS

Both SO filters are originally formulated based on a set of initial orbital elements at t_0 and consider the evolution of these elements over a 5-day time, accounting for zonal perturbations. However, manoeuvres can alter these orbital elements during the analysed period.

One technique to account for the impact of manoeuvres is to sample ephemeris data, as demonstrated in previous works by Casanova et al. in [4] or Woodburn et al. in [22]. Instead of applying the filter solely at t_0 , it is recalculated at regular intervals (Δt) to update the orbital elements and capture the effects of manoeuvres.

The analysed time span is then divided into n intervals, with $\Delta t = \frac{t_f - t_0}{n}$. The orbital elements are updated using ephemeris data at t_k , where $0 \leq k \leq n - 1$. Since these filters account for the evolution of the orbital elements due to zonal harmonics, not only the initial time is relevant, but also the time interval. To determine the boundaries within any interval, $[t_k, t_{k+1}]$, the filter is applied twice:

1. At t_k , considering a forward time span of Δt , as per the original formulation, to obtain r_{max}^k and r_{min}^k .
2. At t_{k+1} , considering a backward time span of Δt , to obtain r_{max}^{k+1} and r_{min}^{k+1} .

The boundaries for this interval are defined as the most restrictive solutions from the two computations:

$$r_{max}([t_k, t_{k+1}]) = \max(r_{max}^k, r_{max}^{k+1}), \quad (17)$$

$$r_{min}([t_k, t_{k+1}]) = \min(r_{min}^k, r_{min}^{k+1}). \quad (18)$$

Using this method, if one of the satellites performs a manoeuvre within $[t_k, t_{k+1}]$, the altitude range defined by the boundaries in Eq. (17) and (18) encompasses the entire range of altitudes of the objects, both before and after the manoeuvre.

Increasing the number of intervals n improves accuracy, especially when manoeuvres occur frequently. However, the computational cost of the filters grows proportionally with n . Thus, determining an optimal value for n is essential. Section 6 presents tests conducted to identify this optimal value.

4 ATMOSPHERIC DRAG MODELING

Atmospheric drag, alongside gravitational harmonics perturbations, is a major source of orbital perturbations for LEO orbits, particularly those below 500 km in altitude. It primarily affects two orbital elements: eccentricity and semimajor axis. In generic orbits, drag reduced both the eccentricity and the semimajor axis by decreasing the apogee radius. However, in nearly circular orbits—such as those of Starlink satellites, which are the focus of this analysis—atmospheric drag primarily causes a gradual reduction in the semimajor axis, leading to a corresponding decay in orbital radius [21]. For this study, the focus is exclusively on this latter effect.

The reduction in orbital radius caused by atmospheric drag is analogous to that of a manoeuvre altering altitude. Consequently, the method introduced to handle manoeuvres can also account for this effect. However, when both effects are combined—for example, when a satellite performs a station-keeping manoeuvre to restore the altitude lost due to the drag—the sampling method cannot fully capture the trajectory using only the initial and final conditions (see e.g. Figure 2).

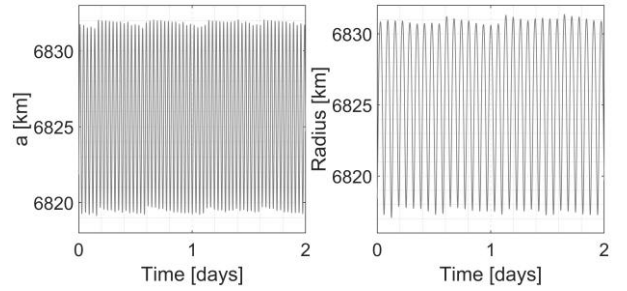


Figure 2 Evolution of the semimajor axis (left) and the radius (right) of NORAD 59427

To address this limitation, the effect of atmospheric drag on the semimajor axis is implemented analytically. Desmond King-Hele, in his book, introduced several theories for calculating changes in orbital elements caused by atmospheric drag. This project employs his model for a spherically symmetric, exponential atmosphere, as detailed in [12].

King-Hele's theory employs the atmospheric density exponential model. This assumes the density of the atmosphere, ρ , decays exponentially from the surface, depending exclusively on the radial distance from Earth's centre. The density variation with altitude is expressed as:

$$\rho = \rho_0 \exp\left(-\frac{r - r_0}{H}\right), \quad (19)$$

where H is the *density scale height*, and ρ_0 is the atmospheric density at a chosen reference altitude, $r = r_0$. These reference values are obtained from the exponential model in Vallado [21], Table 7-4.

In this theory, two variables are introduced: $x = ae$, and $z = \frac{ae}{H}$. The change in the semi-major axis over one orbital period, Δa , is expressed as

$$\Delta a = -2\pi F \cdot BC a^2 \rho_{p0} \exp(\beta(a_0 - a - x_0)) \left[I_0 + 2eI_1 + \frac{3}{4}e^2(I_0 + I_2) + \frac{1}{4}e^3(3I_1 + I_3) + O(e^4) \right], \quad (20)$$

where I_x represents the Bessel function of order x , with argument z ; ρ_{p0} is the atmospheric density at perigee altitude; F represents the factor accounting for atmospheric rotation and BC means the ballistic coefficient.

The factor F is considered constant over one orbital period for a given satellite and is defined as

$$F = \left(1 - \frac{r_p w}{v_p} \cos \hat{i} \right)^2, \quad (21)$$

where r_p, v_p are the radius and velocity at perigee, and w is the angular velocity of the atmosphere.

The ballistic coefficient, BC , is given by:

$$BC = \frac{SC_D}{m}, \quad (22)$$

where S is the cross-sectional area perpendicular to the direction of motion, C_D is the drag coefficient, and m is the mass of the object. The BC values are unknown for most catalogue object and studies on this coefficient are mainly related to the estimation of the drag coefficient, for spherical objects of known surface properties. However, in the entire catalogue, there are many objects for which area and mass are also unknown, particularly most debris objects. Then, this work employs the method presented in [19], which estimate BC values of LEO space objects. Here, ephemeris data are employed rather than two-line element data as in the original method. This method is summarized in Section 4.1 for the reader's convenience.

Assuming that the semimajor axis variation is negligible over a single orbital period, a can be treated as constant within one period, so $a = a_0$. An iterative process is then used to compute the semimajor axis evolution over the analysed time span,

$$a_i = a_{i-1} + \Delta a_{i-1}. \quad (23)$$

Figure 3 illustrates an example of this approximation using the data of NORAD 32259. a means the osculating semi-major axis, \hat{a} the mean one and a_{KH} is the evolution computed analytically.

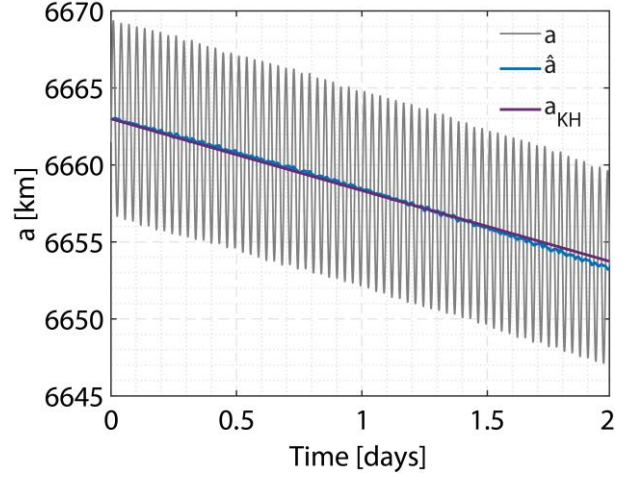


Figure 3 Evolution of the osculating and mean semi-major axis and the analytical approximation of object NORAD 32259

Atmospheric drag impacts the radius function evaluation, requiring its adjustment. Since the trend is monotonically decreasing over time, only the initial, which is \hat{a} , and the final values, which is the analytical value computed at the end of the interval, let us call it a_{KH} for simplicity, are relevant. Particularly, in the original algorithm, that the time interval starts on an initial time and goes forward, the maximum value of the semimajor axis is \hat{a} and the minimum value is a_{KH} . Then, when the equation of the radius is evaluated at $(\hat{\theta}_{min}^*, \beta_{min}^*)$ to compute the minimum radius, the value employed for the semimajor axis is a_{KH} . Thus, the boundaries of the filters are as follow,

$$r_{max} = r(\hat{\theta}_{max}^*, \beta_{max}^*, \hat{a}), \quad (24)$$

$$r_{min} = r(\hat{\theta}_{min}^*, \beta_{min}^*, a_{KH}). \quad (25)$$

where $r(\hat{\theta}, \beta, \hat{a})$ refers to Eq. (2) in the case of the SO-filter and to Eq. (9) in case of the SOP-filter, with \hat{a} as an input variable rather than a constant.

4.1 Estimation of ballistic coefficient

The method developed in [1919] estimates BC values of LEO space objects based on their historical two-line elements. In this work, the method is adapted by utilizing ephemeris data instead of TLEs. The algorithm can be summarized as follows:

The rate of change of the semi-major axis due to atmospheric drag is expressed as:

$$\frac{da}{dt_{Drag}} = \frac{2a^2 v}{\mu} \hat{v}_{Drag} \cdot e_v, \quad (26)$$

where v is the velocity of the object, e_v is the unit vector in the direction of the motion. The vector \hat{v}_{Drag} is the acceleration of the object due to atmospheric drag,

which is defined as,

$$\dot{\mathbf{v}}_{Drag} = \frac{1}{2} \rho BC |\mathbf{v} - \mathbf{V}|^2 \mathbf{e}_{v-V}, \quad (27)$$

where \mathbf{v} is the velocity vector of the satellite, \mathbf{V} is the atmospheric wind velocity vector, and \mathbf{e}_{v-V} is the unit vector of the relative motion respect to the atmospheric wind. Since the effect of atmospheric rotation is already accounted for via the coefficient F , we assume $\mathbf{V} = \mathbf{0}$, $\mathbf{e}_{v-V} = \mathbf{e}_v$.

Assuming that BC is constant. Substituting Eq. (27) into Eq. (26) and integrating, the ballistic coefficient can be expressed as:

$$BC = -\frac{\mu \Delta a_{t_1, Drag}^{t_2}}{\int_{t_1}^{t_2} a^2 v^3 \rho dt}. \quad (28)$$

The denominator is approximated using numerical integration, resulting in:

$$BC = -\frac{\mu \Delta a_{t_1, Drag}^{t_n}}{\sum_{q=1}^{n-1} a_q^2 v_q^3 \rho (t_{q+1} - t_q)}, \quad (29)$$

where a_q and v_q are the osculating semimajor axis and velocity obtained from the ephemeris at time t_q . The time step for the numerical integration, $(t_{q+1} - t_q)$, is determined by the ephemeris resolution, which in this work is set to one minute. The atmospheric density is computed using the exponential model and the variation of the semimajor axis is given by

$$\Delta a_{t_1, Drag}^{t_n} = \hat{a}_{t_n} - \hat{a}_{t_1}, \quad (30)$$

where \hat{a}_{t_1} and \hat{a}_{t_n} represent the mean semimajor axes at times t_1 and t_n , respectively.

5 IMPLEMENTATION OF THE SPACE OCCUPANCY FILTERS

One of the primary differences between the classical application of the SO filters and the current formulation lies in the time of application. In the classical implementation, the filters are applied only at the initial instant of time. In contrast, this formulation applies the filters at regular intervals of Δt , dividing the total time window into n equal intervals,

$$[t_k, t_{k+1}], \quad k \in [0, n-1].$$

Let $r_k(\hat{\theta}, \beta, \hat{a})$ denote the radius expression for the SO-filter (SOP-filter), defined by Eq. (2) (Eq. (9)), using the ephemeris data at t_k as initial condition.

The first step in both filters is to compute the mean orbital elements, $(\hat{a}^k, \hat{e}^k, \hat{i}^k, \hat{\Omega}^k, \hat{\omega}^k, \hat{M}^k)$, using the Kozai-Lyddane equations [13, 15]. Subsequently, the parameters of Cook's theory, defined by Eqs. (3-8) (Eqs. (10-16)) for the SO-filter (SOP-filter), are computed based on these mean orbital elements.

The implementation details of the SO-filter are presented in Section 5.1, while the difference required for the implementation of the SOP-filter are discussed in Section 5.2.

5.1 SO-filter implementation

The algorithm is applied in the same manner across all intervals. For each interval, the filter is applied twice:

1) First Application at t_k :

At time t_k , the filter computes the maximum and minimum values of the function $r_k(\hat{\theta}, \beta, \hat{a})$, considering $\beta \in [\alpha^k, \alpha^k + \kappa^k (\tau_{k+1} - \tau_k)]$. Using the SO-filter algorithm described in [17], the coordinates at which the maximum and minimum radii occur are computed: $(\hat{\theta}_{max}^k, \beta_{max}^k)$, and $(\hat{\theta}_{min}^k, \beta_{min}^k)$.

The evolution of the semimajor axis is then calculated as described in Section 4. Specifically, the maximum value of the semimajor axis is \hat{a}^k , and the minimum value is determined analytically at the end of the interval, denoted as a_{KH}^k . The boundaries of the radius for this interval are then defined as:

$$r_{max}^k = r_k(\hat{\theta}_{max}^k, \beta_{max}^k, \hat{a}^k), \quad (31)$$

$$r_{min}^k = r_k(\hat{\theta}_{min}^k, \beta_{min}^k, a_{KH}^k). \quad (32)$$

2) Second Application at t_{k+1} :

For the second application, the filter is applied at t_{k+1} . It is important to note that the time interval in this case is $[t_{k+1}, t_{k+1} - \Delta t]$, meaning time runs backward. Consequently, the minimum value of the semimajor axis is \hat{a}^{k+1} , and the maximum value is the one computed analytically at the end of this interval $(t_{k+1} - \Delta t)$, denoted as, a_{KH}^{k+1} . The boundaries for this interval are defined as:

$$r_{max}^{k+1} = r_k(\hat{\theta}_{max}^{k+1}, \beta_{max}^{k+1}, a_{KH}^{k+1}), \quad (33)$$

$$r_{min}^{k+1} = r_k(\hat{\theta}_{min}^{k+1}, \beta_{min}^{k+1}, \hat{a}^{k+1}). \quad (34)$$

3) Defining the Interval Boundaries:

The overall boundaries of the orbital radius within $[t_k, t_{k+1}]$ are determined as follows:

$$r_{max,k} = \max(r_{max}^k, r_{max}^{k+1}), \quad (35)$$

$$r_{min,k} = \max(r_{min}^k, r_{min}^{k+1}). \quad (36)$$

For a pair of space objects, the following interval is defined for each object ($i = 1, 2$):

$$\mathcal{R}_i^k = [r_{min,k}^i, r_{max,k}^i]. \quad (37)$$

4) Filter condition:

A conjunction is deemed impossible if:

$$\mathcal{R}_1^k \cap \mathcal{R}_2^k = \emptyset \quad \forall k \in [0, n-1], \quad (38)$$

In this case, the pair is flagged as *negative* and excluded from further analysis. Otherwise, it is flagged as *positive*, requiring more detailed evaluation.

Finally, these intervals can be expanded by applying a buffer, as defined in [18].

5.2 SOP-filter implementation

The implementation of the SOP-filter follows the same steps as the SO-filter, with the key difference that, among all the values of the argument of latitude, only the relative nodes are considered. Instead of defining a single interval that encompasses the entire radius, two separate intervals are introduced for each object and each pair: one corresponding to a relative node,

$$\mathcal{R}_i^k = [r_{min,k}^i, r_{max,k}^i]. \quad (39)$$

and another corresponding to the opposite relative node,

$$\mathcal{R}_i^{k*} = [r_{min,k}^{i*}, r_{max,k}^{i*}]. \quad (40)$$

For a pair of space objects, the filtering condition is given by:

$$\mathcal{R}_1^k \cap \mathcal{R}_2^k = \emptyset \wedge \mathcal{R}_1^{k*} \cap \mathcal{R}_2^{k*} = \emptyset \quad \forall k \in [0, n-1] \quad (41)$$

If this condition holds, the pair is flagged as *negative* and excluded from further analysis, as a conjunction between the two objects is deemed impossible. Otherwise, it is flagged as *positive* for further evaluation.

This filter employs two different types of buffers: a *radial buffer*, which enlarges the radius intervals \mathcal{R} , and an *angular buffer*, which expands the intervals defining the location of the relative nodes. Both are detailed in Section 5.3 of [17].

To test and evaluate the performance of the proposed improvements, five different configurations of the filters are considered:

1. “Original configuration”: The filters are applied as originally described in [18] and [17], without incorporating the improvements presented in this work.
2. “Start-end (1 interval, no drag)”: The time window is not divided, meaning only one interval is considered; and the improvement of atmospheric drag is not considered. In summary:

$$n = 1 \ \& \ a_{KH} = \hat{a} = cte.$$

3. “Start-end (1 interval, with drag)”: The time window is not divided, meaning one interval is considered; the improvement of atmospheric drag is included: $n = 1$.
4. “Daily (2 intervals, with drag)”: The filters are

evaluated every 24 hours, meaning the time window is divided into two intervals ($n = 2$); and atmospheric drag is considered.

5. “12-hourly (4 intervals, with drag)”: The filters are evaluated every 12 hours, dividing the time window into four intervals ($n = 4$); with atmospheric drag included.

6 RESULTS

The modifications developed in Sections 3 and 4 for both the SO-filter and the SOP-filter have been tested and validated using the Starlink constellation, applying the five configurations as outlined in the previous section. The ephemeris of this constellation was obtained from publicly available files from Space Track, with data spanning from 2024-11-07 for two days. The dataset contains information on 5,369 satellites. However, since not all the data start at the same time, the initial epoch of the ephemeris was set at $t_0 = 11 - 07 - 2024, 05:42:42$, which is the earliest time at which data for all satellites are available. Additionally, the data covers the period from t_0 to $t_0 + 42h$, so the time window was set to 42 hours.

The performance of the proposed improvements is assessed using the metrics introduced in Section 6.1. Furthermore, since the ballistic coefficient of each satellite in the constellation must be estimated, Section 6.2 outlines the application of the method presented in Section 4.1 for estimating BC, along with the results for the Starlink constellation. Finally, Section 6.3 presents the results from applying the SO-filter across the five different configurations described above, and Section 6.4 presents the results for the SOP-filter.

6.1 Performance metrics

In order to evaluate the performance of the different configurations of the filters, two definitions are particularly relevant.

A *false positive* occurs when the filter flags a pair as positive because condition (38) or (41) is not satisfied, but the pair is determined to be negative from the result of the complete ephemeris.

A *false negative* occurs when the filter flags a pair as negative because condition (38) or (41) is satisfied, but the pair is determined to be positive from the result of the complete ephemeris. False negatives are the type of error that are not allowed in conjunction analysis, as they can lead to a collision. Therefore, the performance of a filter is considered good if the number of false negatives is reduced to zero and the number of false positives is minimized.

To assess the performance of the different configurations with the number of false positives and false negatives, three different metrics are employed,

following [18].

The *false positives to true positives ratio* is defined as

$$\rho_{fp} = \frac{N_{fp}}{N_{tp}}, \quad (42)$$

where N_{fp} and N_{tp} represent the number of false and true positives, respectively.

The *false negatives to true positives ratio* is defined as

$$\rho_{fn} = \frac{N_{fn}}{N_{tp}}, \quad (43)$$

where N_{fn} is the number of false negatives.

Finally, the *filter effectiveness* defined as

$$\eta = \frac{N_{out}}{N}, \quad (44)$$

where N_{out} is the number of pairs eliminated by the filter because they are flagged as negative, and N is the total number of pairs over which the filter is tested. As the number of satellites employed in this analysis is 5,369, the total number of pairs over which the first filter is tested is 14,410,396.

6.2 Starlink ballistic coefficient

The algorithm described in Section 4.1 to estimate the ballistic coefficient has been applied to the Starlink constellation. For this computation, it is not necessary to have overlapping time windows between satellites, so all available data, spanning two days, are considered.

For a proper estimation of this magnitude, the trajectories must be free of manoeuvres. However, Starlink satellites performs manoeuvres very often. Therefore, an initial analysis was conducted on the slope of the mean semimajor axis to identify intervals where the semimajor axis exhibited a decreasing trend. For those satellites with multiple manoeuvres-free windows, the ballistic coefficient has been computed as the average of the values obtained from each interval. Figure 4 shows the evolution of the osculating semimajor axis and the mean semimajor axis (magenta line). The magenta-shaded regions indicate the manoeuvres-free intervals, while the dots represent the initial and final values of the mean semimajor axis, \hat{a}_{t_1} and \hat{a}_{t_n} . The value of the BC employed in this case is $1.669e-07 \text{ m}^2/\text{kg}$, the average of the values of the four intervals.

Conversely, for objects performing manoeuvres throughout the entire time interval, the ballistic coefficient could not be estimated. There were 100 such cases in the survey.

Figure 5 presents the BC plotted against eccentricity, with the colour bar indicating the different Starlink generations (information sourced from DISCOSweb).

Moreover, Table 1 summarizes the key characteristics of these generations.

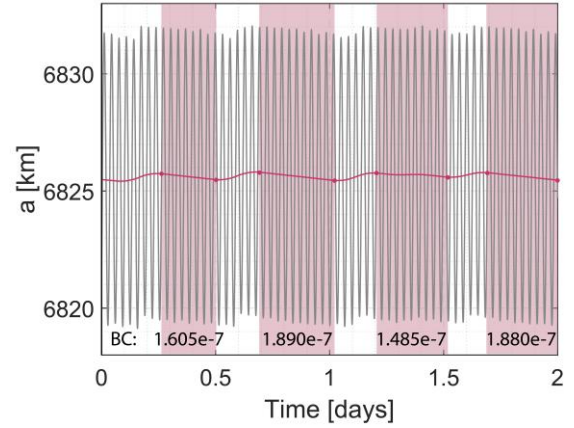


Figure 4 Semimajor axis of NORAD 59427 indicated the intervals selected to compute the BC. The values of the BC are in $[\text{m}^2/\text{kg}]$.

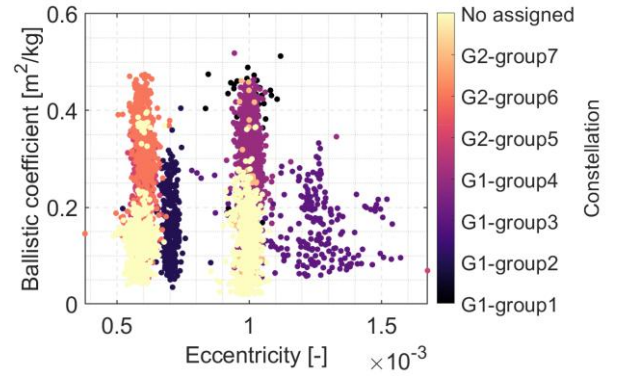


Figure 5 BC of satellites at nominal altitude versus eccentricity.

Table 1 Starlink constellations data from DISCOSweb

| Constellation Name | i (deg) | Deploy Start | Area (m^2) | Mass (kg) |
|--------------------|-----------|--------------|-----------------------|-----------|
| G1-P1-group1 | 53 | 24/05/2019 | 13.56 | 258.96 |
| G1-P1-group2 | 70 | 14/09/2021 | 12.34 | 282.16 |
| G1-P1-group3 | 97.6 | 24/01/2021 | 13.09 | 267.57 |
| G1-P1-group4 | 53.2 | 13/11/2021 | 13.40 | 260.00 |
| G2-P1-group5 | 43 | 28/12/2022 | 11.93 | 292.18 |
| G2-P1-group6 | 43 | 27/02/2023 | 33.88 | 750.00 |
| G2-P1-group7 | 53 | 22/08/2023 | 33.88 | 750.00 |

Although satellites of the same generation share characteristics, no definitive conclusion can be drawn about the ballistic coefficient, therefore, it must be estimated for each object.

6.3 SO-filter performance

Since the SO-filter is the first filter in the process, it is tested against the entire constellation of 5,369 objects, thus, the total number of pairs over which this filter is tested is 14,410,396.

Table 2 shows the number of objects for which the boundaries computed by the filter failed in one or both limits. It is important to note that an object being out-of-bounds does not necessarily imply a false negative in this particular analysis, but it can lead to a false negative when considering other objects.

Table 2 Objects out-of-bound for each configuration of the SO-filter.

| Configuration | Out-of-Bound |
|---------------|--------------|
| Original | 280 |
| 2d no drag | 0 |
| 2d drag | 0 |
| Daily drag | 0 |
| 12h drag | 0 |

Table 3 and Table 4 summarize the performance of each configuration of the filter. The first table presents real positives along with false positives and false negatives, while the second table shows the performance of the different configurations through the three previously defined metrics.

Table 3 Summary of the SO-filter performance comparison.

| Configuration | Real Positives | False Positives | False Negatives |
|---------------|----------------|-----------------|-----------------|
| Original | 3,409,518 | 118,561 | 9,966 |
| 2d no drag | 3,409,518 | 125,901 | 0 |
| 2d drag | 3,409,518 | 132,986 | 0 |
| Daily drag | 3,373,864 | 167,393 | 0 |
| 12h drag | 3,287,200 | 238,178 | 0 |

Note that the false positives for the SO-filter increased as the number of intervals grew. On the other hand, the number of real positives decreased, and the total number of discarded pairs increased. This issue with false positives is due to cases where, considering the total maximum and minimum ephemeris data, the boundaries overlapped. However, when using intervals, the boundaries did not overlap. Despite this, since the objects are very close, the filter still detected them as positives.

Table 4 Summary of the SO-filter performance with metrics.

| Configuration | ρ_{fp} | ρ_{fn} | η |
|---------------|-------------|-------------|---------|
| Original | 3.488 % | 0.293 % | 75.59 % |
| 2d no drag | 3.693 % | 0 % | 75.47 % |
| 2d drag | 3.900 % | 0 % | 75.42 % |
| Daily drag | 4.990 % | 0 % | 75.56 % |
| 12h drag | 7.282 % | 0 % | 75.65 % |

The configuration *Start-end (2 days, no drag)* is able to eliminate all false negatives and bound correctly all the objects. This shows that for the SO-filter, there is no need to improve the treatment of atmospheric drag. Regarding the number of intervals, when it increases, the percentage of discarded pairs also increases, though the improvement is not significant. The percentage of discarded pairs increases only 0.23% between one and four intervals. Since the computational time of the filter is multiplied by the number of intervals, it is not worth increasing it by a factor of four, for such a small improvement. Thus, the best configuration for the SO-filter is the *Start-end method (2 days, no drag)*.

These results, obtained with a real population, are highly consistent with those obtained using the numerical propagation presented in [17]. The number of eliminated pairs is reduced by only 2%, while the metric of the false positives increases by the same margin of 2%. These are excellent results, demonstrating the filter's robustness and suitability for transitioning from theoretical simulations to a real-world population.

6.4 SOP-filter performance

Since the SOP-filter is the second stage of the process, it is assessed using the pairs flagged as positives by the SO-filter. The number of pairs that pass through the chosen configuration of the SO-filter, *Start-end (2 days, no drag)* is 3,542,504. However, as this filter cannot handle coplanar pairs, because the MOID can be far from the relative nodes, those pairs whose mutual inclination is smaller than 10 degrees or higher than 170 degrees are not considered for the analysis. Thus, the SOP-filter is evaluated employing 3,303,697 pairs.

Table 5 shows the number of objects for which the boundaries computed by the filter failed in one or more of the limits.

Table 5 Objects out-of-bound for each configuration of the SOP-filter.

| Configuration | Out-of-Bound |
|---------------|--------------|
| Original | 285,758 |

| | |
|------------|---------|
| 2d no drag | 159,026 |
| 2d drag | 169 |
| Daily drag | 0 |
| 12h drag | 0 |

Table 6 and Table 7 summarize the performance of each configuration of the SOP-filter. The first one presents real positives along with false positives and false negatives, while the second one shows the performance of the different configurations through the three previously defined metrics.

Table 6 Summary of the SOP-filter performance comparison.

| Configuration | Real Positives | False Positives | False Negatives |
|---------------|----------------|-----------------|-----------------|
| Original | 2,066,021 | 36,393 | 12,732 |
| 2d no drag | 2,066,021 | 56,208 | 7,135 |
| 2d drag | 2,066,021 | 137,873 | 0 |
| Daily drag | 2,062,071 | 118,122 | 0 |
| 12h drag | 2,053,835 | 107,658 | 0 |

Table 6 shows that, for the SOP-filter, it is necessary to consider the improvement in atmospheric drag to completely avoid false negatives errors. Thus, the configuration chosen for the SO-filter is not an option in this second filter.

Table 7 Summary of the SOP-filter performance with metrics.

| Configuration | ρ_{fp} | ρ_{fn} | η |
|---------------|-------------|-------------|---------|
| Original | 1.772% | 0.620 % | 36.75 % |
| 2d no drag | 2.730 % | 0.347 % | 35.98 % |
| 2d drag | 6.673 % | 0 % | 33.29 % |
| Daily drag | 5.728 % | 0 % | 34.01 % |
| 12h drag | 5.242 % | 0 % | 34.57 % |

The same conclusion can be drawn about the number of intervals. The percentage of discarded pairs increased with the number of intervals, but not in a significant manner to justify the increase in the computational time. However, even though the number of false negatives is zero in all configurations that account for the improvement in atmospheric drag, the *Start-end (2 days, drag)* configuration presents 169 cases of poorly bounded objects. These objects could potentially result in false negatives with other objects do not consider in this analysis. Therefore, as in conjunction analysis the

safer option is always preferred, the *Daily (2 intervals, no drag)* is the one recommended for the SOP-filter.

In contrast to the first filter, the performance of the SOP-filter in this series is notably affected when tested on a real population. This could be due to the finer nature of the filter, which makes it more susceptible to perturbations, or possibly due to the specific population chosen for testing. Nevertheless, considering the complete process, the number of pairs is reduced from 14,410,396 to 2,458,451 by the SO and SOP-filters. Thus, only around 17% of the input pairs need further analysis.

7 CONCLUSIONS AND FUTURE WORK

This project evaluates the performance of the SO- and SOP-filters against real data, emphasizing the need for adjustments to account for satellite manoeuvres and atmospheric drag. It proposes a sampling method to manage manoeuvres that alter the satellite's altitude, as well as an analytical approach to incorporate the semimajor axis decay, and consequently the radius decay, caused by the atmospheric drag.

These improvements were tested on the Starlink constellation by running the filters under five different configurations to evaluate both methods. The analysis concludes that while the SO-filter only requires adjustments for handling manoeuvres, the SOP-filter also necessitates the inclusion of the atmospheric model. The SO-filter performs effectively considering only a single interval; however, the SOP-filter needs to consider at least two intervals. In addition, increasing the number of intervals yields a marginal improvement in discarded pairs at the expense of significantly higher computational time, thus, the minimum number of intervals required for each filter is chosen.

The filtering process eliminates 83.2% of the total input pairs from further analysis, with no false negatives detected. This substantial reduction in the number of pairs has significant implications for space traffic management and collision risk mitigation.

Future work will include the incorporation of a safety buffer to account for out-of-plane manoeuvres, which may affect the relative nodes calculation in the SOP-filter. A more in-depth analysis of these manoeuvres is needed to better capture their impact on the filter's performance. Additionally, to generalize the filters for broader use in the LEO region, a more comprehensive atmospheric model should be considered, taking into account not only the effect of drag on the semimajor axis but also its influence on eccentricity. Finally, the integration of a third filtering stage based on the satellite phase, such as the classical time filter, could provide further improvements in this filtering process.

ACKNOWLEDGEMENTS

The authors gratefully acknowledge support by grant TED2021-132099B-C33 funded by MICIU/AEI/10.13039/501100011033 and by “European Union NextGenerationEU/PRTR.”. Ana S. Rivero was funded by a FPU grant from the Spanish Ministry of Universities.

REFERENCES

1. Alfano, S. (2012). Toroidal path filter for orbital conjunction screening. *Celestial Mechanics and Dynamical Astronomy*, **113**(3):321–334.
2. Alfano, S., & Finkleman, D. (2014). On selecting satellite conjunction filter parameters. *Acta Astronautica*, **99**, 193–200.
3. Bombardelli, C., Falco, G., Amato, D., & Rosengren, A.J. (2021). Space occupancy in low-earth orbit. *Journal of Guidance, Control, and Dynamics*, **44**(4):684–700.
4. Casanova, D., Tardioli, C., and Lemaître, A. (2014). Space debris collision avoidance using a three-filter sequence. *Monthly Notices of the Royal Astronomical Society*, **442**(4):3235–3242.
5. Cook, G. E. (1966) Perturbations of near-circular orbits by the earth’s gravitational potential. *Planetary and Space Science*, **14**(5):433–444.
6. Cook, R. A. (1992) The long-term behaviour of near-circular orbits in a zonal gravity field. *Advances in the Astronautical Sciences*, **76**:2205–2221.
7. Escobar, D., Águeda, A., Martín, L. & Martínez, F.M. (2012). Efficient all vs. all collision risk analyses. *Journal of Aerospace Engineering, Sciences and Applications*, **4**(2), 446–48.
8. Gronchi, G. F. (2003) On the stationary points of the squared distance between two ellipses with a common focus. *SIAM Journal on Scientific Computing*, **24**(1):61–80.
9. Gronchi, G. F. (2005) An algebraic method to compute the critical points of the distance function between two keplerian orbits. *Celestial Mechanics and Dynamical Astronomy*, **93**:295–329.
10. Hoots, F. R., Crawford, L. L., and Roehrich, R. L. (1984). An analytic method to determine future close approaches between satellites. *Celestial Mechanics*, **33**(2):143–158.
11. Kerr, E. and Sánchez Ortiz, N. (2021) State of the art & future needs in conjunction analysis methods, processes and software. In *Proceedings of the 8th European Conference on Space Debris* (virtual), Darmstadt, Germany, 20–23 April 2021, 2021.
12. King-Hele, D. (1987). *Satellite orbits in an atmosphere. Theory and applications*.
13. Kozai, Y. (1959). The motion of a close earth satellite. *The Astronomical Journal* **64**:367–377.
14. Kozai, Y. (1962). Second-order solution of artificial satellite theory without air drag. *The Astronomical Journal* **67**, 446–461.
15. Lyddane, R. H. (1963). Small eccentricities or inclinations in the brouwer theory of the artificial satellite. *The Astronomical Journal*, **68**(8):555–558.
16. Muelhaupt, T.J., Marlon, E.S., Morin, J. & Wilson, R.S. (2019). Space traffic management in the new space era. *Journal of Space Safety Engineering*, **6**(2):80–87.
17. Rivero, A. S., Baù, G., Vazquez, R., and Bombardelli, C. (2024). A novel conjunction filter based on the minimum distance between perturbed trajectories. URL: arXiv:2410.20928.
18. Rivero, A. S., Bombardelli, C., and Vazquez, R. (2024). Short-term space occupancy and conjunction filter. URL: arXiv:2309.02379.
19. Sang, J., Bennett, J. C., and Smith, C. H. (2013). Estimation of ballistic coefficients of low altitude debris objects from historical two-line elements. *Advances in Space Research*, **52**(1):117–124.
20. Stevenson, E., Rodriguez-Fernandez, V., Urrutxua, H. & Camacho, D. (2023) Benchmarking deep learning approaches for all-vs-all conjunction screening. *Advances in Space Research*, **72**(7):2660–2675.
21. Vallado, D. A. (2001). *Fundamentals of astrodynamics and applications*. Volume 12. Springer Science & Business Media.
22. Woodburn, J., Coppola, V., and Stoner, F. (2009). A description of filters for minimizing the time required for orbital conjunction computations. In *AAS/AIAA Astrodynamics Conference*.